Topologically protected flatness in chiral moiré heterostructures

Valentin Crépel,[1] Peize Ding,[2] Nishchhal Verma,[2] Nicolas Regnault,[3,4] and Raquel Queiroz[1,2]

[1] *Center for Computational Quantum Physics, Flatiron Institute, New York, NY 10010, USA*
[2] *Department of Physics, Columbia University, New York, NY 10027, USA*
[3] *Laboratoire de Physique de l'École normale supérieure, ENS, Université PSL, CNRS, Sorbonne Université, Université Paris-Diderot, Sorbonne Paris Cité, 75005 Paris, France*
[4] *Department of Physics, Princeton University, Princeton, NJ 08544, USA*

The observation of delicate correlated phases in twisted heterostructures of graphene and transition metal dichalcogenides suggests an inherent resilience of moiré flat bands against certain types of disorder. We investigate the robustness of moiré flat bands in the chiral limit of the Bistrizer-MacDonald model, applicable to both platforms in certain limits. We show a drastic difference between the protection of the first magic angle and higher magic angles to chiral symmetric disorder such as random higher moiré potential harmonics arising, for instance, from lattice relaxation. We find that the first magic angle is topologically protected by a topological index theorem, similar to the protection of the zeroth Landau level of Dirac fermions, whose flatness withstands any chiral symmetric perturbation such as non-uniform magnetic fields. Focusing on the first magic angle of twisted bilayer graphene, our analysis reveals a hidden non-local constant of motion that permits the decomposition of the non-abelian gauge field induced by inter-layer tunnelings into two decoupled abelian ones, underscoring a topological mechanism for band flatness. Through numerical simulations, we further show the strikingly different robustness of flat bands across protected (first) and unprotected (higher) magic angles in the presence of various types of disorder and identify the scattering processes that are enhanced or suppressed in the chiral limit. Interestingly, we find that the suppression of disorder broadening persists away from the chiral limit and is further accentuated by isolating a single sublattice polarized flat band in energy. Our analysis suggests the Berry curvature hotspot at the top of the K and K' valence band in the transition metal dichalcogenide monolayers is essential for the stability of its moiré flat bands and their correlated states.

I. INTRODUCTION

The recent observation of the fractional quantum anomalous Hall effect in twisted monolayers of $MoTe_2$ marks the first unequivocal evidence of topologically ordered states in quantum material without external magnetic fields [1–4]. It paves the way for realizing non-abelian states of matter through superconducting coupling [5–14], which are essential for the development of topologically protected quantum computing [15]. However, topologically ordered states are typically fragile to perturbations. The original fractional quantum Hall effect in GaAs was only observed for extremely high mobility samples [16]. In comparison, transition metal dichalcogenides (TMDs), such as $MoTe_2$, are not necessarily clean monolayers. Their mobility usually lies two orders of magnitude below that of typical samples of GaAs that host fractional quantum Hall states [17–21]. Additionally, strain, lattice relaxation, and twist angle variations are expected to further disorder the heterostructures built from these monolayers [22–26]. Nonetheless, fractional Chern insulators [27–29] were observed in both twisted $MoTe_2$ homobilayers and twisted bilayer graphene (TBG) at finite field [30]. This unexpected observation hints at the possibility that these heterostructures carry some intrinsic protection to a disorder that enables the realization of such delicate, strongly correlated phases.

In this work, we ask the question: Can the flatness of moiré flat bands be itself topologically protected? A hint towards an answer follows from the pioneering work by Aharonov and Casher [31], who showed that a relativistic Dirac particle in a magnetic field has exactly Φ/Φ_0 zero modes of definite chirality, where Φ is the total magnetic flux through the lattice, and Φ_0 the flux quantum. As a consequence, the zeroth Landau level of a Dirac particle remains perfectly flat even when the magnetic field is non-uniform. This perfect immunity against certain forms of disorder is tied to a chiral anomaly and a topological index that protects the net chirality of the system [32]. The anticommuting chiral symmetry relates states of opposite energies, allowing the assignment of a proper chirality to all zero energy states, such as the zeroth Dirac Landau level. These states with definite chirality must remain strictly at zero energy, even in the presence of disorder, as long as the chiral symmetry is preserved. The same anomaly guarantees that the previous theory cannot be realized on a lattice since the total chirality of fermions on a lattice must vanish [33]. Therefore, a chiral Landau level must only appear as a surface theory [34] or within a valley isolated in momentum space. The latter scenario is relevant for the K valley in both graphene [35] and TMDs [36]. The chiral anomaly has remarkable consequences when it comes to the effect of disorder in the Landau levels of these materials: Provided the disorder does not couple the two Dirac valleys of opposite chirality, their zeroth Landau level is not broadened by disorder, unlike every other Landau level at a finite energy [37]. A similar result is expected for Lan-

dau levels of quadratic bands, provided their $g-$factor is exactly two resulting from the Berry curvature at the band edge [38]. No anomaly or chiral Landau levels are expected for a gas of free electrons under a magnetic field, such as in GaAs.

With an external magnetic field, which is typically homogeneous, the additional protection due to the chiral anomaly has limited consequences. Only a slight broadening difference is seen in experiment between the zeroth and higher Landau levels in graphene [39]. In fact, in Hall systems, the protection by a chiral anomaly has little physical importance because the Landau level spread to cyclotron gap ratio can be efficiently reduced by going to larger magnetic fields. Contrast this with moiré materials, where there is no external magnetic field but rather a fictitious gauge field that arises from highly non-uniform interlayer couplings and where the spectral gap around the band of interest cannot be arbitrarily increased using an external experimental knob, and the protection provided by the index theorem can play a crucial role.

In this paper, we explore the protection of flat bands in moiré bilayers endowed from the chiral anomaly in the chiral limit of the Bistrizer-MacDonald model of TBG [40, 41], which has also been shown to be an insightful limit for twisted TMDs upon adding a mass to the Dirac theory of each monolayer [42], and may also apply to other types of heterostructures [43–47]. This limit permits a formal map between the flat bands at the magic angle and Landau levels under a pseudo, non-abelian gauge field $\vec{\mathcal{A}}$. Naively, we should expect that these states are *not* protected by the index theorem, which is only applicable when the gauge field is abelian (Sec. II). Remarkably, we discover that for large angles, including the first magic angle, there is a hidden non-local symmetry that allows for the decomposition of the $SU(2)$ gauge field into two decoupled abelian components $U(1) \times U(1)$ (Sec. III). Applied specifically to the chiral limits of TBG and twisted $MoTe_2$, this large-angle abelian regime corresponds to twist angles $\theta \gtrsim 0.7°$ and $\theta \gtrsim 2.1°$, respectively. In the decoupled basis, electrons feel a non-uniform and periodic magnetic field B'. The matching of the magnetic length introduced by B' and the moiré length approximates well the magic condition, as anticipated in Ref. [48] where it was understood as a consequence of the topological Atiyah-Singer index theorem [49, 50]. This leads to striking qualitative differences in the robustness of the different magic angles against chiral preserving disorder that we numerically investigate in Sec. IV by introducing random higher harmonics of the moiré interlayer tunneling potential. We note that our analysis captures the effect of lattice corrugations and strain introduced at the moiré unit cell edges, which is particularly important at small twist angles. We find that the first magic angle is mostly undisturbed by higher harmonics, which makes it possible to consistently define the same magic angle condition throughout the sample despite small deformations at sub-moiré length scales. Importantly, this is not true for higher magic angles, suggesting that it may be impossible to observe higher magic angles in realistic experimental settings, which agrees with asymptotic calculations [51].

II. INDEX THEOREM

A highly counter-intuitive property of the zero-energy Landau level of Dirac particles in a magnetic field was simultaneously discovered by Aharonov and Casher [31] and Dubrovin and Novikov (who considered the square of the Dirac Hamiltonian) [38]: it remains *perfectly flat* and extensively degenerate for *arbitrary non-uniform* magnetic fields provided the total magnetic flux threading the system is a constant. This strikingly contrasts the behavior of all higher Landau levels of the same system and those stemming from quadratic bands, which in similar settings acquire a dispersion proportional to the non-uniformity of the magnetic field.

The perfect immunity of the zeroth Landau level to magnetic field variations has since then been interpreted as a consequence of a topological index theorem [32] formulated by Atiyah and Singer (AS) for Dirac operators coupled to arbitrary (multi-dimensional) gauge fields in even dimensions [49, 50]. The two-dimensional version with matrix valued gauge field $\vec{\mathcal{A}} = (\mathcal{A}_x, \mathcal{A}_y)$ relevant for the present study states that the operator

$$\mathcal{H}_{\rm D} = \begin{bmatrix} 0 & \mathcal{D}^\dagger \\ \mathcal{D} & 0 \end{bmatrix}, \quad \mathcal{D} = -2i\mu_0\partial_{\bar{z}} + \mathcal{A}_z, \tag{1}$$

with $2\partial_{\bar{z}} = \partial_x + i\partial_y$, $\mathcal{A}_z = \mathcal{A}_x + i\mathcal{A}_y$ and μ_0 the identity with the same size as $\mathcal{A}_z$, is subject to the topological anomaly

$$\dim\,(\mathrm{Ker}\;\mathcal{D}) - \dim\,(\mathrm{Ker}\;\mathcal{D}^\dagger) = \int_S \frac{\mathrm{Tr}\mathcal{B}}{2\pi}, \tag{2}$$

where S is the compact surface on which $\mathcal{H}_{\rm D}$ is defined, and $\mathcal{B} = \vec{\nabla} \times \vec{\mathcal{A}} + [\mathcal{A}_x, \mathcal{A}_y]$ denotes the curvature corresponding to the gauge field, *i.e.* the magnetic field strength. The block structure in Eq. 1 is provided by the anticommuting chiral symmetry that Dirac Hamiltonian enjoys in even dimensions.

The topological nature of the AS theorem is clear: it only depends on the integrated magnetic flux but not on the local details and variation of $\mathcal{B}$. The right-hand side of Eq. 2 is nothing but the Chern number of the electromagnetic connection, or gauge field, with which the reader may be more familiar in the context of Berry connection/curvature [52] (to avoid confusion, we stress that these two Chern numbers are *a priori* unrelated and that the "topology" of the AS theorem is distinct from to band topology). The most direct physical consequence of the AS theorem is that the number of zero modes of $\mathcal{H}_{\rm D}$ is *independent of* local variations of the gauge potential $\vec{\mathcal{A}}$ and of the metric of the Dirac operator. This is equivalently stated: the density of states at zero energy is topologically protected against all perturbations

of the Hamiltonian anti-commuting with the chiral operator. In the case of graphene in a magnetic field, these perturbations physically correspond to strain and lattice corrugations [37, 53].

The AS index also protects the zeroth Landau level of systems with quadratic dispersion provided they can be written down as the square of $\mathcal{H}_{\rm D}$ up to an overall sublattice dependent uniform potential [38, 54]. For particles in a magnetic field, this condition is equivalent to having a $g-$factor exactly equal to 2. In other contexts, it can lead to spin-orbit-like corrections to the quadratic Hamiltonian [42].

III. APPLICATION TO CHIRAL TBG

In this section, we introduce the chiral model for TBG and prove that, for sufficiently large angles, it can be analytically decoupled into two independent Dirac Hamiltonians of the form of Eq. 1 coupled to abelian gauge fields. The flat bands appearing in this abelian regime correspond to the first (experimentally observed) magic angle, whose existence can be understood as a consequence of the AS theorem. We contrast this behavior with higher (theoretically predicted) magic angles, which we show are not topologically protected by the index theorem in Eq. 2 due to their nodal structure. This difference has important consequences regarding the robustness of the flat bands, investigated in Sec. IV.

A. Interlayer tunneling as a fictitious gauge field

We consider the chiral limit of the Bistritzer-MacDonald model for TBG [40, 41], which in the basis $\{(A,t),(A,b),(B,t),(B,b)\}$, with A/B and t/b the sublattice and layer degrees of freedom respectively described by $\vec{\sigma}$ and $\vec{\mu}$ Pauli matrices, and in valley-K reads

$$\frac{\mathcal{H}}{|v\kappa|}=\begin{bmatrix}0 & \mathcal{D}^\dagger\\ \mathcal{D} & 0\end{bmatrix},\quad \mathcal{D}=-2i\mu_0\partial_{\bar z}+\alpha\mathcal{A}_z, \tag{3}$$
$$\mathcal{A}_z=A_z^{(1)}\mu_1+A_z^{(2)}\mu_2,\quad \alpha=\frac{w}{|v\kappa|},$$
$$A_z^{(1)}=\sum_{n=0,1,2}\omega^n\cos(\kappa_n\cdot r),\quad A_z^{(2)}=\sum_{n=0,1,2}\omega^n\sin(\kappa_n\cdot r),$$

with κ_n the $2\pi n/3$-rotation of the κ corner of the moiré Brillouin zone aligned with the negative y-axis, $|\kappa|=2|K|\sin(\theta/2)$, v the Fermi velocity of graphene, and where α measures the strength of AB tunneling w in unit of the typical moiré kinetic energy $|v\kappa|$. The Hamiltonian in the other valley is obtained by time-reversal conjugation.

The suggestive form of Eq. 3 makes it clear that AB interlayer tunnelings in chiral TBG act as a fictitious gauge potential for the two coupled Dirac cones with chiral symmetry σ_3 [55]. Furthermore, the chiral model

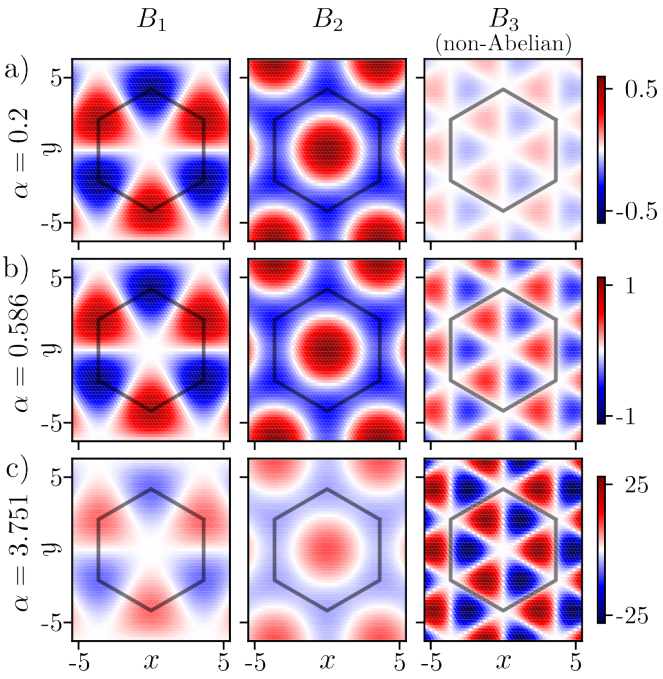

FIG. 1. The three components of the SU(2) fictitious magnetic field strength $\mathcal{B}=B_1\mu_1+B_2\mu_2+B_3\mu_3$ induced by interlayer tunneling for a small $\alpha=0.2$ (a), the first magic angle $\alpha=0.586$ (b), and the second magic angle $\alpha=3.751$ (c). The different α-scaling of the abelian $B_{j=1,2}=\alpha\vec{\nabla}\times\vec{A}^{(j)}$ and non-abelian $B_3=2\alpha^2\vec{A}^{(1)}\times\vec{A}^{(2)}$ components causes a transition from a weakly non-abelian regime ($\alpha\lesssim 1$) to a deeply non-abelian one ($\alpha\gtrsim 1$). The grey hexagon shows the $\sqrt{3}\times\sqrt{3}$ enlarged moiré unit cell over which the tunneling terms are periodic.

Eq. 3 is known to host perfectly flat bands at zero energy for $\alpha=0.586, 2.221, 3.751,\cdots$ [56]. In that context, it is natural to wonder whether these exact flat bands are topologically protected by the index theorem of Eq. 2 or not [48, 57]. At first sight, the answer to this question seems to be negative. Indeed, $\mathcal{A}_z$ physically comes from inter-layer tunneling and is entirely carried by off-diagonal layer Pauli matrices. As a result of the trace in Eq. 2, the index corresponding to this gauge field must vanish. In fact, this is a generic feature of SU(N) gauge fields with $N>1$, whose generators are all traceless.

We notice that the fictitious gauge field is almost abelian for small values of α (see Fig. 1). This becomes clear if we split the fictitious field strength $\mathcal{B}=\mathcal{B}_{\rm ab}+\mathcal{B}_{\rm nab}$ into abelian $\mathcal{B}_{\rm ab}$ and non-abelian $\mathcal{B}_{\rm nab}$ components, which respectively read

$$\mathcal{B}_{\rm ab}=B_1\mu_1+B_2\mu_2,\quad B_{j=1,2}=\alpha\vec{\nabla}\times\vec{A}^{(j)},$$
$$\mathcal{B}_{\rm nab}=B_3\mu_3,\quad B_3=2\alpha^2\vec{A}^{(1)}\times\vec{A}^{(2)}. \tag{4}$$

One of the crucial points of this paper is that the abelian and non-abelian parts of $\mathcal{B}$ do not scale with the same power of α. As a result, the system is almost abelian for small α, *i.e.* for large twist angles, while it is almost entirely non-abelian for large α, *i.e.* small angles.

We illustrate this difference in Fig. 1, where we plot the magnetic strength $B_{1,2,3}$ for a small $\alpha = 0.2$, and at the two first magic angles $\alpha = 0.586$ and 3.751.

The weakly non-abelian case, for $\alpha \ll 1$, bears similarity with that of electrons evolving in an underlying non-colinear spin texture producing an effective $SU(2)$ gauge field [58, 59]. In the adiabatic limit where the spin texture slowly varies in space, the system split into two decoupled components, respectively aligned and anti-aligned with the underlying texture, that each experience an abelian gauge potential [60–62]. Similar adiabatic approximations have been used in different moiré systems to approximate the inter-layer tunneling as an effective $U(1)$ abelian gauge field [63, 64]. For a quantitative description of the physics, the domain of validity of this adiabatic approximation should be identified, and all the correcting terms should be explicitly included.

The near-abelian gauge field observed for small α in Fig. 1 hints at a similar decoupling, thereby separating two distinct regimes in the physics of TBG: an abelian one for $\alpha \lesssim 1$ in which the AS index theorem can topologically protect a flat band, and a non-abelian one for $\alpha \gtrsim 1$ where no topological protection occurs and flat bands are accidental.

B. Hidden constant of motion

We now make the distinction between the abelian and non-abelian regime analytically precise by proving that an invertible transformation can decouple the Hamiltonian of chiral TBG (Eq. 3) into two independent abelian $U(1)$ Dirac operators, for which the AS index theorem applies, so long as $\alpha < 0.89$.

Our goal is to find the α for which there exists an invertible transformation U, making the Dirac operator abelian or diagonal; in other words, we want

$$\mathcal{D}' = U^{-1}\mathcal{D}U = -2i\mu_0\partial_{\bar{z}} + A'_z\mu_3, \tag{5}$$

for some A'_z. When such a U exists, we notice that $[\mu_3, \mathcal{D}'] = 0$, such that the original Dirac operator possesses a hidden constant of motion $[U\mu_3U^{-1}, \mathcal{D}] = 0$. Conversely, if $\mathcal{D}$ has a constant of motion of the form $\vec{X}\cdot\vec{\mu}$, then the matrix $U = N^{-1/2}(\vec{X}\cdot\vec{\mu} + x\mu_3)$, with $N = 2x(x + X_3)$ and $x^2 = \vec{X}\cdot\vec{X}$, provides the desired invertible operator for Eq. 5 to hold. Referring to App. A for a detailed derivation, we find that the abelian gauge field and field strength are then related to $\vec{X}$ by

$$A'_z = A'_x + iA'_y = \frac{\alpha(\vec{X}\cdot\vec{\mathcal{A}})}{x + X_3}, \quad B' = \vec{\nabla}\times\vec{A}'. \tag{6}$$

It is, therefore, sufficient to solve for a periodic hidden constant of motion $\vec{X}$ satisfying $[\vec{X}\cdot\vec{\mu}, \mathcal{D}] = 0$. We rewrite this condition as

$$\partial_{\bar{z}}\vec{X} = \alpha M\vec{X}, \quad M_{ij} = \varepsilon_{ikj}A_z^{(k)}, \tag{7}$$

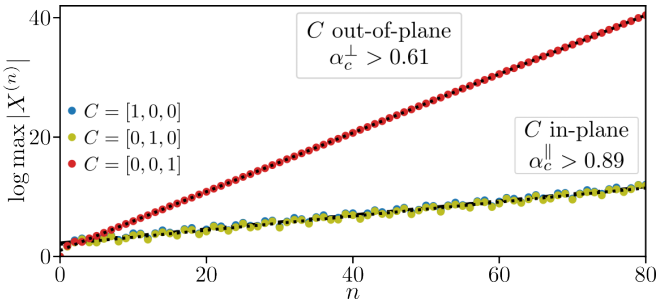

FIG. 2. Maximum of the n-th coefficient of the α-Taylor series of the constant of motion $\vec{X}$, in logarithmic scale, for different integration constants C. The slopes of the linear fit for $n > 10$ (dotted lines) provide the constant p_C that allows to lower bound the radius of convergence of the Taylor series. These lower bounds are indicated in boxes.

with ε_{ijk} the Levi-Civita tensor. Note that the matrix M and the vector $\vec{X}$ have complex entries. The fact that this hidden constant of motion is complex is imposed by symmetry. If $\vec{X}$ were real, we could add $(\vec{X}\cdot\mu)\sigma_3$ to the Hamiltonian and energetically separate the two flat bands at the magic angle of chiral TBG while preserving all the symmetries of the Hamiltonian, in direct contradiction with the topology of the bands at zero energy [65]. Note also that the antisymmetry of the Levi-Civita tensor in Eq. 7 implies that x^2 is uniform, while the symmetry of the chiral TBG Hamiltonian ensures that it is real; a demonstration of these facts is given in App. A. Being interested in the small α limit, we look for solutions as a Taylor series $\vec{X} = \sum_{n=0}^{\infty}\alpha^n\vec{X}^{(n)}$, whose components must satisfy the recurrence relation $\partial_{\bar{z}}X^{(0)} = 0$ and $\partial_{\bar{z}}X^{(n+1)} = MX^{(n)}$ for $n \geq 0$. Solving this recurrence relation yields

$$X^{(n)} = I^{(n)}(M)C, \quad I(f) = P\left[\int \mathrm{d}\bar{z}\,(Mf)\right], \tag{8}$$

where $P[f] = f - \mathrm{mean}(f)$ removes the uniform part of the periodic function f, $I^{(n)}(M) = I\circ I\circ\cdots\circ I\circ I(M)$ denotes I composed n-times (with $I^{(0)}$ the identity), while C is an unconstrained integration constant. Numerically, we evaluate the matrix multiplication by M in real space but perform the anti-holomorphic integration in reciprocal (momentum) space, using fast Fourier transforms to switch from one representation to another efficiently.

The explicit solution of Eq. 8 allows us to determine for which α the hidden constant of motion exists by calculating the radius of convergence of the series that defines $\vec{X}$. To that end, we compute the ℓ_∞-norm of the $\vec{X}^{(n)}$ term and find their asymptotic behavior at large n. The results are shown in Fig. 2, where we observe that the norms asymptotically grow with n as power laws: $\max|\vec{X}^{(n)}| \sim e^{np_c}$ with p_C a real coefficient corresponding to the fitted linear slopes in Fig. 2. The radius of convergence α_c of the series defining $\vec{X}$ is then lower bounded by e^{-p_c}. Because the uniform vector C can

be arbitrarily chosen, we have repeated the calculation for $C = [1, 0, 0]$, $C = [0, 1, 0]$ and $C = [0, 0, 1]$. In the two first cases, where the C is in-plane, we find an identical radius of convergence $\alpha_c^{\parallel} > 0.89$; while the third case, where C lies out-of-plane, gives $\alpha_c^{\perp} > 0.61$. In practice, any uniform vector C will lead to a constant of motion using Eq. 8, which we can therefore construct for all $\alpha < \max(\alpha_c^{\parallel}, \alpha_c^{\perp})$.

We have arrived at one of our main results: for $\alpha < 0.89$, it is possible to recast the chiral Hamiltonian of TBG as two decoupled Dirac Hamiltonian feeling opposite *abelian* magnetic field $\pm B'$ (see Eq. 6). The effective magnetic field B' is represented in Fig. 3a-c for different values of α using our numerical solution for the constant of motion $\vec{X}$. Using graphene's Fermi velocity and typical values of the inter-layer tunneling and AB sites in TBG, the identified abelian regime corresponds to twist angles $\theta > 0.7°$, which only includes the first magic angle.

C. Topologically protected magic angle

Within the identified abelian regime ($\alpha < 0.89$), we can use the AS theorem to predict the emergence of topologically protected flat bands. The only technical subtlety is to identify the minimal compact integration surface S containing all independent fermionic degrees of freedom of the theory to avoid double counting the zero modes [48]. Using the translation and C_{2y} symmetries of TBG, we identify this minimal surface with the half moiré unit cell depicted in Fig. 3c with a dashed triangle.

The index theorem (Eq. 2) ensures the existence of a perfectly flat and topologically protected band when the flux Φ of B' through S reaches an integer multiple of 2π [48]. In Fig. 3d, we show the numerically evaluated value of this flux as a function of α. We observe that, although B' becomes more and more localized as α grows (Fig. 3a-c), its maximum value also increases and so does its integrated flux. The flux Φ reaches 2π for $\alpha^* = 0.581$, which agrees to less than a percent with the exact value of Ref. [56]. We attribute this difference to the limited numerical accuracy of our calculations as α approaches $\alpha_c^{\perp}$. Indeed, the number of terms necessary for the Taylor series to converge increases as α grows, *e.g.* it reaches ~ 200 for $\alpha = 0.5$. At this point, the coefficients admixed when numerically solving for the recurrence $I^{(n)}(M)$ differ by more than fifteen orders of magnitudes (which can be seen by extrapolation of Fig. 2 to $n = 200$), which corresponds to our numerical accuracy.

Let us finally mention that the counting of flat bands agrees with the one expected for twisted bilayer graphene [40, 41]. Indeed, under the decoupling of Eq. 5, we can split $\mathcal{D}' = \mathcal{D}'_+ \otimes \mathcal{D}'_-$ into two independent abelian Dirac operators feeling opposite gauge field $\mathcal{D}'_\pm = -2i\partial_{\bar{z}} \pm A'_z$. As a result, when $\Phi = 2\pi$ at $\alpha = \alpha^*$, the AS theorem ensures the existence of *two* topologically protected flat bands. One is fully localized on the A sublattice and is spanned by zero modes of $\mathcal{D}'_+$, and the other flat band lives on the B sublattice and is spanned by zero modes of $\mathcal{D}'^{\dagger}_-$. The two sets of zero modes are related to one another by the C_{2y} symmetry of the chiral TBG Hamiltonian.

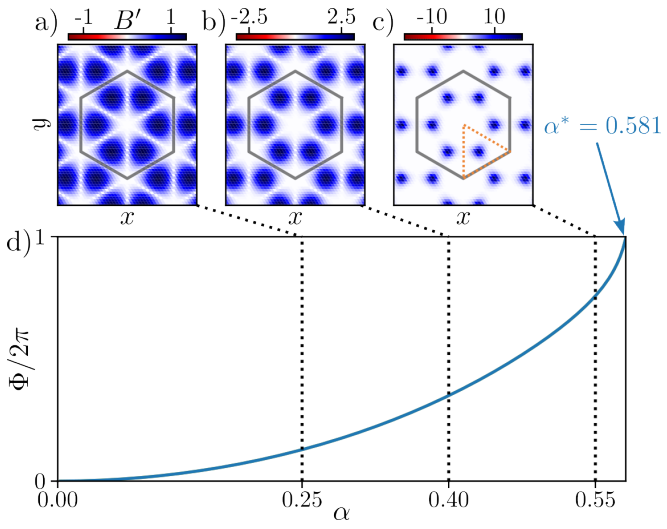

FIG. 3. Magnetic field strength $B' = \vec{\nabla} \times \vec{A}'$ after abelianization with C =[0,0,1] for $\alpha = 0.25$ (a), $\alpha = 0.4$ (b) and $\alpha = 0.55$ (c); the real-space boundaries are the same as in Fig. 1. The minimal integration surface S containing all independent fermionic degrees of freedom of the theory is shown as a dotted triangle in (c). d) Flux of B' through S as a function of α. The Atiyah-Singer index ensures the existence of a flat band when this flux Φ reaches 2π. In our calculations, this occurs at $\alpha^* = 0.581$. We used 512 points along each primitive vector of the moiré Brillouin zone.

In essence, the invertible transformation U of Eq. 5 allows us to define layer-spinors that everywhere follow the direction of the fictitious gauge field $\mathcal{A}_z$ created by the AB inter-layer tunneling. This decoupling generically relies on an adiabatic approximation, whose region of validity has been analytically identified by explicit computation of the radius of convergence of the small-α Taylor series defining the layer-spinors.

D. No anomaly for higher magic angles

We have explicitly constructed an invertible transformation decomposing the chiral model of TBG into two independent abelian components for $\alpha < 0.89$ by a Taylor expansion in α, enabling us to interpret the flat band at the first magic angle as topologically protected by the AS index theorem. This construction hints that higher magic angles $\alpha = 2.221, 3.751, \cdots$ are not topologically protected as they lie deep in the non-abelian regime (see Fig. 1). However, it is unclear whether these flat bands are genuinely accidental, *i.e.* not protected by an index, or if they are topologically protected but the abelianization of the theory involves a transformation U that cannot be expressed as a Taylor series in α. Here, we

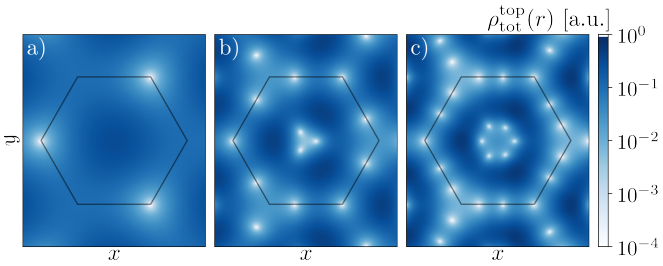

FIG. 4. Total density in the top layer $\rho^{\text{top}}_{\text{tot}}(r)$ of the flat band polarized on the A sublattice at the (a) first $\alpha = 0.586$, (b) second $\alpha = 2.221$, and (c) third $\alpha = 3.751$ magic angles. The main difference between (a) and (b-c) is the existence of nodes away from the origin and corners of the Wigner-Seitz moiré unit cell (shown in black) for the higher magic angles.

show that the former is true.

We rely on the known physical difference between the first and the higher magic angle flat bands of chiral TBG: their nodal structure. The total layer-polarized density of the higher magic angle flat bands is indeed known to possess nodes away from the center and corners of the Wigner-Seitz moiré unit cell ($AA/AB/BA$ points), as shown in Fig. 4 [66]. At these points, the flat-band eigenvectors are fully layer polarized, and the transformation matrix U, if it existed, would be entirely carried by μ_3. At a nodal point r_0 different of the center and corners of the moiré Wigner-Seitz cell, we would then have $\vec{X}(r_0) \cdot \vec{\mu} = x\mu_3$, which we show is impossible in App. A if we want to preserve a uniform value of x since both $\vec{A}_1$ and $\vec{A}_2$ are non-zero at generic point r_0 of the moiré unit cell. The presence of nodes in the total layer-polarized density of the flat band of the smaller magic angles prevents the abelianization of the theory. It ensures that the higher magic α possesses accidental (unprotected) flat bands. This lack of robustness deep in the non-abelian regime of chiral TBG ($\alpha > 1$) agrees with recent mathematical large-α asymptotic results [51] and earlier numerical observations [23].

IV. EFFECT OF DISORDER

In the previous section, we identified two types of flat bands in chiral TBG: the topologically protected ones of the first magic angle ($\alpha < 0.89$) and the accidental ones appearing at higher magic angles ($\alpha > 0.89$). Here, we study their behaviors in the presence of disorder by building a hierarchy between the various possible disorder channels and analyzing how the flat band responds to them. Our results, summarized in Tab. I, are finally substantiated by numerical simulations.

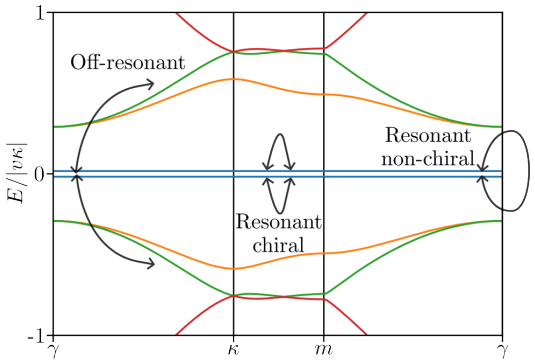

FIG. 5. Schematic representation of the different disorder channels considered, *e.g.* in Tab. I, using the band structure of chiral TBG at the first magic angle along a high-symmetry line of the moiré Brillouin zone. The two zero-energy sublattice-polarized flat bands have been shifted in energy for visibility.

A. Hierarchy between disorder channels

As represented in Fig. 5, we split the various types of disorder susceptible to broaden the flat bands of chiral TBG into three categories: the off-resonant terms scattering particles from the flat-band to degrees of freedom above or below the spectral gap, the chiral terms that anticommute with the abelian chiral symmetries of the two flat bands (they can only be defined for the first magic angle, see Sec. III), and resonant non-chiral scattering processes directly coupling the two sublattice polarized flat-bands. In this paragraph, we identify what physical mechanism, if any, protects the flat bands against those three types of disorders.

Off-resonant channels protected by the spectral gap: Disorder channels of the first kind connect the flat bands to degrees of freedom away from zero energy. Included in this category is, for instance, inter-layer tunneling that preserves the sublattice. Suppose the disorder strength is small compared to the spectral gap separating the flat bands from the rest of the spectrum. In that case, such disorder only contributes to the bandwidth of the flat band to second order, thereby granting an effective protection of the flat band against off-resonant scattering terms. Because the spectral gap separating the flat bands from the rest of the spectrum exponentially decays with α for large α [67], we expect that higher magic angles will be more susceptible to off-resonant disorder than the abelian flat band of the first magic angle. This is especially significant because the decay of the spectral gap is found to be extremely steep: the gap above the flat bands of the three first magic angles $\alpha = 0.586, 2.221, 3.751$ is respectively equal to 0.29, 0.059 and 0.0027 in units of the typical moiré kinetic energy $|v\kappa|$ (that itself decreases linearly with θ). The asymptotic scaling of the spectral gap for large α was recently used to prove the impossibility of observing very small magic angles in chiral TBG [51].

channel	example	abelian ($\alpha < 0.89$)	non-abelian ($\alpha > 0.89$)
off-resonant	AA/BB-tunneling	protected by spectral gap	smaller gap (exponentially small in α [67])
chiral	homo-strain	protected by AS index	not protected by an index
resonant, non-chiral $\mu_{1,2}$	AB-tunneling	protected by localization near AA	weakly protected (less localized)
resonant, non-chiral μ_3	hetero-strain	not protected	weakly protected by nodes near AA

TABLE I. Effect of the different disorder channels on the flat bands in the abelian ($\alpha < 0.89$) and non-abelian ($\alpha > 0.89$) regimes. Off-resonant terms connect the flat bands to degrees of freedom above the spectral gap, chiral terms anti-commute with the abelian chiral symmetry of both flat bands, while non-chiral resonant term scatter particles between the two flat bands and are assumed to preserve C_3 on average (Fig. 5). The second and third columns summarize if the flat bands are protected from the different types of disorder and, if so, by which physical mechanism: either scattering is suppressed by a spectral gap, the AS index, or because the wavefunctions are localized in real space, and the disorder matrix elements are suppressed.

Topologically protected channels: Another difference between the first and higher magic angles is the presence of an index theorem, derived in Sec. III, which has direct consequences on the robustness of the flat bands against another type of disorder (which can be both off-resonant and resonant). Indeed, the topological nature of the AS theorem ensures perfect immunity of the flat bands of the first magic angle against disorder channels that simultaneously anticommute with the chiral symmetries of the two abelian Dirac operators $\mathcal{D}'_{\pm}$ (Sec. II). Because of the U transformation, these two chiral symmetries are not exactly equal to the chiral operator σ_3 of the original Hamiltonian Eq. 3, but to its projection onto the two abelian sectors. Therefore, the perturbations that leave the two flat bands intact must simultaneously anticommute with σ_3 and commute with the constant of motion $\vec{X} \cdot \vec{\mu}$. The only channels of disorder complying with these constraints are $\sigma_{1/2}\mu_0$ and $\sigma_{1/2}(\vec{X} \cdot \vec{\mu})$. The former represents a homo-strain that identically couples to both layers. The latter is a fine-tuned combination of interlayer tunneling and heterostrain. In practice, any realistic disorder will contain some non-zero weight onto these two topologically protected channels, further lowering the overall strength of the bandwidth-generating part of the disorder for the first magic angle.

Localization protected channels: We now turn to resonant scattering channels between the two sublattice-polarized flat bands and first consider those carried by the off-diagonal layer Pauli matrices $\mu_{1,2}$, *e.g.* higher harmonics of the AB interlayer tunneling. Any inter-layer term of this form preserving C_3 symmetry must vanish at the AA stacking point. If the disorder only preserves C_3 on average, and if it does not fluctuate too wildly over the moiré scale (*i.e.* if the disorder auto-correlation distance is not too small compared to the moiré lattice constant), it will remain strongly suppressed in the AA region. Now, the wavefunctions of the first magic angle flat bands in chiral TBG are known to be strongly peaked around the AA point [68–70]. Due to additional nodes near the AA region, higher magic angles have their density localized closer to the regions where the inter-layer resonant disorder is strong [66], which can be seen in Fig. 4 (note the logarithmic scale). A direct consequence of this fact is a lower sensitivity of the first magic angle to inter-layer resonant disorder, *i.e.* an effective protection from the localization of the wavefunction.

Unprotected channels: At last, we consider resonant intra-layer disorder, corresponding, for instance, to hetero-strain. These disorder channels can have large amplitude near the AA region if they preserve C_3 on average. The previous argument is therefore reversed, and we now expect higher magic angles having nodes near the AA region to enjoy a lower sensitivity to this disorder. On the other hand, the first magic angle is expected to be very sensitive to hetero-strain. This has indeed been observed numerically, with the landscape of quantum phases stabilized by interactions drastically changing upon including hetero-strain of very weak amplitude [71–74].

To summarize (see Tab. I), the first magic angle possesses an intrinsic robustness to a broad class of disorder channels thanks to its topological origin, large gap, and the localization of its wavefunctions. It is, however, sensitive to hetero-strain, which can lead to substantial changes in the quantitative physics of TBG [75]. On the other hand, higher magic angles are expected to strongly broaden in the presence of any disorder except intra-layer resonant channels.

B. Numerical simulations

To solidify these observations, we numerically simulate the effect of disorder in the chiral model of TBG. The role of the AS index in the robustness against disorder can be further highlighted by focusing on disorder in the AB inter-layer tunneling channel, for which all magic angles possess some protection due to the localization of their wavefunctions and where the first magic angle enjoys an additional protection due to its abelian nature (third line of Tab. I).

To be more concrete, we introduce a C_3 symmetric disorder by adding higher-order harmonics to the inter-layer tunneling potential. This amounts to the substitution

$\mathcal{A}_z \to \mathcal{A}_z + \delta\mathcal{A}_z$ in Eq. 3 with

$$\delta\mathcal{A}_z = \sum_{m=1}^{m_c} \mu_m (a^{(1)}_{m,z}\mu_1 + a^{(2)}_{m,z}\mu_2), \qquad (9)$$
$$a^{(1)}_{m,z} + i a^{(2)}_{m,z} = \sum_n e^{i(\kappa_{m,n}\cdot r + \phi_{m,n})},$$

where $\kappa_{m,0}$ is the m-th smallest vector in the first trine of the plane that connects the two corners κ and κ' of the moiré Brillouin zone (up to reciprocal lattice vectors), $\kappa_{m,n}$ denotes its rotation by $2n\pi/3$, and μ_m stands for the amplitude of the m-th harmonic. The $\phi_{m,n}$ phases are included such that $\delta\mathcal{A}_z$ does not break C_3 and the C_{2y} symmetry of Eq. 3. The precise definition of all these terms is given in App. B. We only consider the first $m_c = 10$ harmonics and discretize $\mathcal{D}$ on a momentum-space lattice containing all plane waves with wavevectors of norm smaller than a certain radius R_k.

For the considered C_3-preserving inter-layer tunneling disorder, the chiral model of TBG still possesses exact magic angles where the bands at zero energy become perfectly degenerate [56, 76]. The precise value of these magic α can be efficiently determined using the method of Refs. [56, 67], where all magic angles are determined as eigenvalues of a carefully designed operator Λ, whose explicit expression is given in App. B for comprehensiveness. We first use this method to characterize the sensitivity of the magic angles to the different harmonics in Eq. 9. For this purpose, we choose one specific harmonic m and compute the change $\delta\alpha$ in the first, second, and third magic angles when $\mu_m = \delta\mu$ is set to a small but finite value (keeping all other $\mu_{n\neq m} = 0$). For small disorder strength, this corresponds to taking the derivatives $\partial\alpha/\partial\mu$ of Λ's eigenvalues with respect to μ_m. We numerically evaluate this derivative using a small enough $\delta\mu = 0.02$, and plot our results for $|\partial\alpha/\partial\mu|$ in Fig. 6a. We observe that the α deviations in the first magic angle exponentially decay with m and are negligible for $m > 5$, indicating that the first magic angle is robust against microscopic details on scales smaller than the moiré length. In contrast, the deviations for the higher magic angle can reach up to ten times the amplitude of the added perturbation and do not decay with m. This suggests that the higher magic angles are easily affected by microscopic disorder at all scales down to graphene's lattice constant. Perturbations on those scales, such as lattice relaxations, are inevitable and necessarily spoil the prediction for higher magic angles [41, 56]. Perturbations on scales larger than the moiré length are also studied in App. C.

To understand the physical implications of the difference in $\delta\alpha$ for first and higher magic angles observed in Fig. 6a, we consider realistic disorder realization containing all harmonics $m \leq m_c$ with amplitudes μ_m drawn uniformly in $[-1, 1]$ with the overall normalization $\sqrt{\sum_m \mu_m^2} = \delta\mu = 0.1$. We plot the distribution of the first three magic angles for 500 realizations of such disorder in Fig. 6b, which shows a similar trend

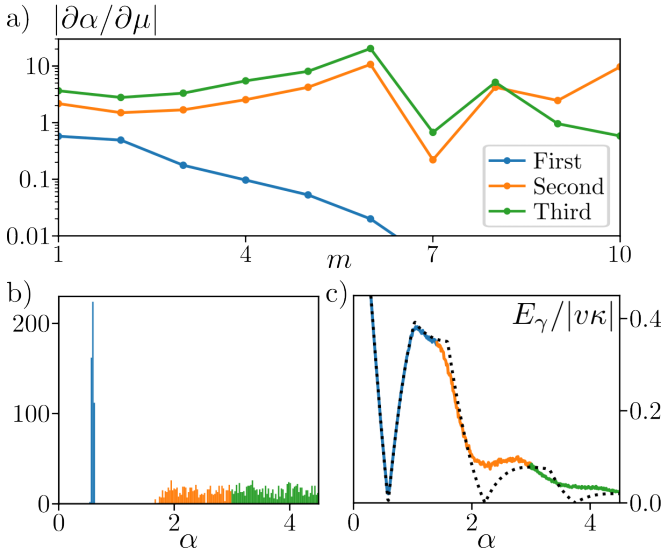

FIG. 6. a) Variation $|\partial\alpha/\partial\mu|$ of the first (blue), second (orange), and third (green) magic angle computed for a small $\delta\mu = 0.02$ perturbation in the m-th harmonics of the AB inter-layer tunneling (see Eq. 9). To obtain converged results for large m, we used a large truncation radius $R_k = 25\sqrt{3}|\kappa|$. b) Histogram of the magic angles for 500 realization of the inter-layer tunneling disorder with all μ_m drawn uniformly and normalized as $\sqrt{\sum_m \mu_m^2} = \delta\mu = 0.1$. c) E_γ, the energy of the top active band crossing zero energy in chiral TBG at the center of the moiré Brillouin zone (γ), averaged over 500 disorder realizations for the same distribution of μ_m as in (b). The dashed line shows the result in the absence of disorder. $R_k = 25\sqrt{3}|\kappa|$ for (b) and $R_k = 10\sqrt{3}|\kappa|$ for (c) is used. Colors are provided as a guide to the eye, allowing us to identify the regions closest to 0.586 (blue), 2.221 (orange), and 3.751 (green), which correspond to the magic angles in the absence of disorder.

as Fig. 6a: the distribution of magic α is sharply peaked around the original value 0.586 for the first magic angle. At the same time, it is extremely broad and featureless for higher magic angles. To interpret this result, picture a sample in which different patches of the sample (different unit cells) are characterized by slightly different atomic arrangements and lattice relaxation profiles that locally change the values of the μ_m. We can assign an effective magic angle α to each of these regions. When TBG is close to the first unperturbed magic angle, the distribution of these magic α is peaked, and the magic condition is almost simultaneously satisfied for all patches (see Fig. 6b). This is not true for higher magic angles, such that the density of states at zero energy is smeared in many patches, yielding a strong broadening of the original flat bands.

We can estimate the flat band broadening by computing E_γ the average energy of the topmost band at the center of the moiré Brillouin zone (γ point) for 500 realizations of the same realistic disorder pattern for a fixed twist angle, *i.e.* as a function α. The results presented in Fig. 6c pictorially capture our previous statement: the

higher magic angles are completely washed out due to their high sensitivity to disorder. The average γ-point energy only displays an apparent non-monotonic behavior with an almost vanishing bandwidth at the first magic angle, which we have seen to be protected against disorder (Tab. I).

Our numerical calculations clearly show that only the flat bands at the first magic angle retain a large density of states in the presence of disorder. As explained in Tab. I, this is due to the combination of the topological protection from the AS theorem, large spectral gap, and strong localization of the wavefunctions in the flat band. Higher magic angles are sensitive to lattice scale details and should be interpreted as accidental artifacts of the continuum model rather than experimentally observable features.

C. Away from the chiral limit

We finally check whether our results, which find their roots in the chiral limit of TBG, also hold in the more realistic situation where non-zero AA tunnelings are included in the Bistritzer-MacDonald model [40]. When the AA tunneling amplitude w_0 is non-zero, we cannot identify the magic angle with the point where the γ-point energy vanishes, as we did in Fig. 6c, since the model never features perfectly flat bands. Instead, we locate the magic angle as the points for which the Fermi velocity at the corner of the moiré Brillouin zone vanishes [40, 76]. We have numerically computed this Fermi velocity $v_m(\alpha)$ averaged over 500 realizations of the generic disorder pattern described above as a function of α, both in the chiral limit $w_0 = 0$ and for the realistic value $w_0 = 0.8w$ [40]. Our results are presented in Fig. 7, where, for better comparison, we have chosen $\delta\mu = 0.1$ for the chiral limit and $\delta\mu = 0.2$ in the realistic regime, leading to the similar average velocity at the first magic angle. In both the chiral and realistic (nonchiral) limits, disorder barely affects the Fermi velocity (blue lines) from its clean values (dotted lines) as long as we are in the abelian regime ($\alpha < 0.86$). In the non-abelian regime, the average velocity deviations become significant. Consequently, only the first magic angle still strongly suppresses the Fermi velocity $v_m(\alpha)$. In contrast, all higher magic angles are washed out by disorder – we interpret this as a direct consequence of the robustness granted by the AS topological index described in the second line of Tab. I.

To understand why a stronger disorder strength is necessary for the realistic limit ($\delta\mu = 0.2$) to obtain the same average value of $v_m(\alpha)$ at the first magic angle than in the chiral limit ($\delta\mu = 0.1$), we should take a closer look at the effect of the non-chiral part of the disorder. More precisely, it is known that the wavefunction of the flat bands is more localized near the AA region in the realistic limit $w_0 = 0.8w$ than in the chiral limit [41]. Therefore, the third line of Tab. I qualitatively captures the better protection of the flat band against inter-layer tunneling disorder.

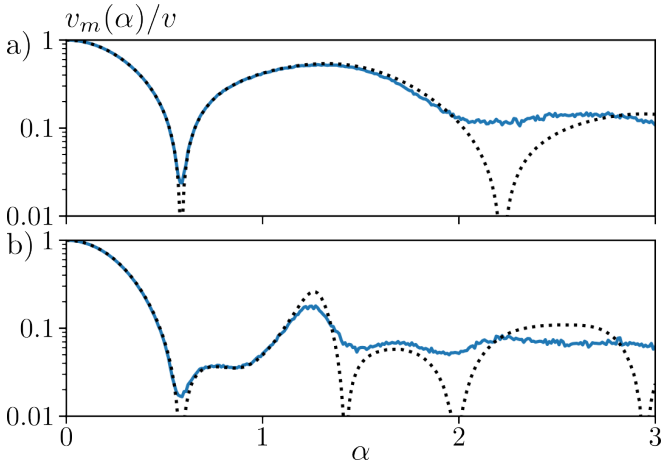

FIG. 7. Fermi velocity at the corner of the moiré Brillouin zone $v_m(\alpha)$ averaged over 500 disorder realizations for the same distribution of μ_m as in Fig. 6, both in the chiral limit (a) and the realistic value for AA tunneling strength $w_0 = 0.8w$ (b). To obtain similar results at the first magic angle, allowing for a fair comparison, we have used $\delta\mu = 0.1$ for the chiral limit (a) and $\delta\mu = 0.2$ in the realistic regime (b). The dashed lines show the same quantity in the absence of disorder. We have normalized the results by the Fermi velocity of graphene v and shown them on a log scale to better discern the effect of the weak disorder.

V. IMPLICATIONS FOR TMDS

While TBG has been the main focus up to now, let us expand on the implications of our results to twisted TMDs, which share the same chiral limit as TBG (Eq. 3) up to the addition of a mass term that describes the gap of the semiconducting monolayers [42]. Most of our analysis, particularly the decoupling into abelian components from Sec. III, goes through in the presence of this mass term. For twisted $MoTe_2$ homobilayers, similar estimates as above show that the physics is effectively abelian for $\theta > 2°$, which lead to topologically protected flat bands at the first magic angles $\theta \sim 3.2°$ [42]. Away from the chiral limit, the resulting flat band will acquire some dispersion due to additional orbital-preserving terms in the Hamiltonian but remain robust against disorder if the results of Fig. 7 can be generalized to twisted $MoTe_2$ homobilayers. The mass term and the strong spin-orbit coupling of TMDs [36] strongly suppress all resonant non-chiral disorder – the only ones that spoil the protection of the flat bands, see Tab I – as they fully lift the degeneracy of the flat band to leave a single topologically protected valence flat band per spin flavor. Twisted TMDs, therefore, are ideal hosts for delicate correlated topological phases of matter. They host weakly dispersing Chern bands fully protected against all forms of disorder thanks to the combinations of the AS topological index theorem

and their spectral gap.

We also note that other approaches aim at interpreting the physics of twisted TMDs as particles moving in an abelian gauge field [63, 64, 77–80]. Our work precisely determines in which regimes and for which angles such a picture is valid.

VI. CONCLUSION

In this work, we have demonstrated that the flat band appearing at the first magic angle in twisted graphene and transition metal dichalcogenides bilayers, both in the chiral limit, can be understood as originating from Dirac particles evolving in an abelian gauge field. Their zero energy Landau levels become perfectly flat and topologically protected against disorder thanks to a topological index theorem when the moiré length and the effective magnetic length of the system match. This description is only possible when the inter-layer tunneling acting as a fictitious gauge field can be adiabatically decoupled into abelian components. Such decoupling occurs for large twist angles where the typical kinetic energy on the moiré scale is not negligible compared to the strength of tunneling and corresponds to $\theta > 0.7°$ for twisted bilayer graphene and $\theta > 2°$ for twisted $MoTe_2$. The topological nature of the zeroth Landau level of chiral Dirac operators has critical consequences on the robustness of the magic angle against perturbations. In particular, we find that only the first magic angle benefits from the enhanced robustness to disorder granted by the Atiyah-Singer topological index. Therefore, we conclude that flat bands appearing at smaller twist angles are accidental, in the sense that they do not have an index and are strongly susceptible to spreading out in energy even for weak disorder on scales smaller than the moiré pattern. Let us finally highlight that all the flat bands at all magic angles are characterized by the same band topology (Chern number, Wannier obstructions, *etc*...) [65, 81], but only for those appearing at the first magic angle, the full Hamiltonian of TBG features an additional Atiyah-Singer topological index protecting the flat band.

VII. ACKNOWLEDGEMENT

Research on topological properties of moiré materials is supported as part of Programmable Quantum Materials, an Energy Frontier Research Center funded by the U.S. Department of Energy (DOE), Office of Science, Basic Energy Sciences (BES), under award DE-SC0019443. The Flatiron Institute is a division of the Simons Foundation. N.R. acknowledges support from the QuantERA II Programme which has received funding from the European Union's Horizon 2020 research and innovation program under Grant Agreement No 101017733.

[1] J. Cai, E. Anderson, C. Wang, X. Zhang, X. Liu, W. Holtzmann, Y. Zhang, F. Fan, T. Taniguchi, K. Watanabe, *et al.*, Nature **622**, 63 (2023).
[2] F. Xu, Z. Sun, T. Jia, C. Liu, C. Xu, C. Li, Y. Gu, K. Watanabe, T. Taniguchi, B. Tong, J. Jia, Z. Shi, S. Jiang, Y. Zhang, X. Liu, and T. Li, Physical Review X **13**, 031037 (2023).
[3] Y. Zeng, Z. Xia, K. Kang, J. Zhu, P. Knüppel, C. Vaswani, K. Watanabe, T. Taniguchi, K. F. Mak, and J. Shan, Nature **622**, 69 (2023).
[4] H. Park, J. Cai, E. Anderson, Y. Zhang, J. Zhu, X. Liu, C. Wang, W. Holtzmann, C. Hu, Z. Liu, *et al.*, Nature **622**, 74 (2023).
[5] R. S. Mong, D. J. Clarke, J. Alicea, N. H. Lindner, P. Fendley, C. Nayak, Y. Oreg, A. Stern, E. Berg, K. Shtengel, *et al.*, Physical Review X **4**, 011036 (2014).
[6] A. Vaezi, Physical Review X **4**, 031009 (2014).
[7] C. Repellin, A. M. Cook, T. Neupert, and N. Regnault, npj Quantum Materials **3**, 14 (2018).
[8] M. Barkeshli, Physical Review Letters **117**, 096803 (2016).
[9] M. Barkeshli and X.-G. Wen, Physical Review B **84**, 10.1103/physrevb.84.115121 (2011).
[10] M. Barkeshli and X.-L. Qi, Physical Review X **2**, 031013 (2012).
[11] V. Crépel, N. Regnault, and B. Estienne, Physical Review B **100**, 125128 (2019).
[12] B. A. Katzir, A. Stern, E. Berg, and N. H. Lindner, arXiv preprint arXiv:2011.13950 (2020).
[13] A. P. Reddy, N. Paul, A. Abouelkomsan, and L. Fu, arXiv preprint arXiv:2403.00059 (2024).
[14] V. Crépel and N. Regnault, arXiv preprint arXiv:2403.05622 (2024).
[15] A. Y. Kitaev, Annals of physics **303**, 2 (2003).
[16] H. L. Stormer, D. C. Tsui, and A. C. Gossard, Reviews of Modern Physics **71**, S298 (1999).
[17] H. C. Movva, A. Rai, S. Kang, K. Kim, B. Fallahazad, T. Taniguchi, K. Watanabe, E. Tutuc, and S. K. Banerjee, ACS nano **9**, 10402 (2015).
[18] H.-J. Chuang, B. Chamlagain, M. Koehler, M. M. Perera, J. Yan, D. Mandrus, D. Tomanek, and Z. Zhou, Nano letters **16**, 1896 (2016).
[19] S. Xu, J. Shen, G. Long, Z. Wu, Z.-q. Bao, C.-C. Liu, X. Xiao, T. Han, J. Lin, Y. Wu, *et al.*, Physical Review Letters **118**, 067702 (2017).
[20] R. Pisoni, T. Davatz, K. Watanabe, T. Taniguchi, T. Ihn, and K. Ensslin, Physical Review Letters **123**, 117702 (2019).
[21] S. Zhao, J. Huang, V. Crépel, X. Wu, T. Zhang, H. Wang, X. Han, Z. Li, C. Xi, S. Pan, *et al.*, arXiv preprint arXiv:2308.02821 (2023).
[22] J. H. Wilson, Y. Fu, S. Das Sarma, and J. H. Pixley, Physical Review Research **2**, 023325 (2020).
[23] S. Carr, S. Fang, Z. Zhu, and E. Kaxiras, Physical Review Research **1**, 013001 (2019).
[24] N. Nakatsuji and M. Koshino, Physical Review B **105**, 245408 (2022).

[25] H. Sainz-Cruz, T. Cea, P. A. Pantaleón, and F. Guinea, Physical Review B **104**, 075144 (2021).
[26] A. Thomson and J. Alicea, Physical Review B **103**, 125138 (2021).
[27] D. Sheng, Z.-C. Gu, K. Sun, and L. Sheng, Nature communications **2**, 389 (2011).
[28] T. Neupert, L. Santos, C. Chamon, and C. Mudry, Physical Review Letters **106**, 236804 (2011).
[29] N. Regnault and B. A. Bernevig, Physical Review X **1**, 021014 (2011).
[30] Y. Xie, A. T. Pierce, J. M. Park, D. E. Parker, E. Khalaf, P. Ledwith, Y. Cao, S. H. Lee, S. Chen, P. R. Forrester, *et al.*, Nature **600**, 439 (2021).
[31] Y. Aharonov and A. Casher, Physical Review A **19**, 2461 (1979).
[32] M. Katsnelson and K. Novoselov, Solid State Communications **143**, 3 (2007).
[33] H. Nielsen and M. Ninomiya, Physics Letters B **105**, 219 (1981).
[34] F. Zhang, C. L. Kane, and E. J. Mele, Physical Review B **86**, 081303 (2012).
[35] K. S. Novoselov, A. K. Geim, S. V. Morozov, D. Jiang, M. I. Katsnelson, I. V. Grigorieva, S. Dubonos, and A. Firsov, nature **438**, 197 (2005).
[36] D. Xiao, G.-B. Liu, W. Feng, X. Xu, and W. Yao, Physical Review Letters **108**, 196802 (2012).
[37] T. Kawarabayashi, Y. Hatsugai, and H. Aoki, Physical Review Letters **103**, 156804 (2009).
[38] B. Dubrovin, S. Novikov, *et al.*, Pisma V Zhurnal Eksperimentalnoi I Teoreticheskoi Fiziki **79**, 1006 (1980).
[39] A. Giesbers, U. Zeitler, M. Katsnelson, L. Ponomarenko, T. Mohiuddin, and J. Maan, Physical Review Letters **99**, 206803 (2007).
[40] R. Bistritzer and A. H. MacDonald, Proceedings of the National Academy of Sciences **108**, 12233 (2011).
[41] G. Tarnopolsky, A. J. Kruchkov, and A. Vishwanath, Physical Review Letters **122**, 106405 (2019).
[42] V. Crépel, N. Regnault, and R. Queiroz, arXiv preprint arXiv:2305.10477 (2023).
[43] E. Khalaf, A. J. Kruchkov, G. Tarnopolsky, and A. Vishwanath, Physical Review B **100**, 085109 (2019).
[44] D. Guerci, P. Simon, and C. Mora, Physical Review Research **4**, L012013 (2022).
[45] X. Wan, S. Sarkar, S.-Z. Lin, and K. Sun, Physical Review Letters **130**, 216401 (2023).
[46] J. Wang and Z. Liu, Physical Review Letters **128**, 176403 (2022).
[47] V. Crépel, A. Dunbrack, D. Guerci, J. Bonini, and J. Cano, Physical Review B **108**, 075126 (2023).
[48] A. Parhizkar and V. Galitski, arXiv preprint arXiv:2301.00824 (2023).
[49] M. F. Atiyah and I. M. Singer, Annals of mathematics , 484 (1968).
[50] M. Atiyah and I. M. Singer, Proceedings of the National Academy of Sciences **81**, 2597 (1984).
[51] S. Becker, I. Oltman, and M. Vogel, arXiv preprint arXiv:2402.12799 (2024).
[52] D. J. Thouless, M. Kohmoto, M. P. Nightingale, and M. den Nijs, Physical Review Letters **49**, 405 (1982).
[53] M. Katsnelson and M. Prokhorova, Physical Review B **77**, 205424 (2008).
[54] B. Estienne, N. Regnault, and V. Crépel, Physical Review Research **5**, L032048 (2023).
[55] J. Liu, J. Liu, and X. Dai, Physical Review B **99**, 155415 (2019).
[56] S. Becker, M. Embree, J. Wittsten, and M. Zworski, Probability and Mathematical Physics **3**, 69 (2022).
[57] Y. Sheffer and A. Stern, Physical Review B **104**, L121405 (2021).
[58] J. Ye, Y. B. Kim, A. J. Millis, B. I. Shraiman, P. Majumdar, and Z. Tešanović, Physical Review Letters **83**, 3737 (1999).
[59] P. Bruno, V. K. Dugaev, and M. Taillefumier, Physical Review Letters **93**, 096806 (2004).
[60] I. Martin and C. Batista, Physical Review Letters **101**, 156402 (2008).
[61] S. Nakatsuji, N. Kiyohara, and T. Higo, Nature **527**, 212 (2015).
[62] N. Verma, Z. Addison, and M. Randeria, Science Advances **8**, eabq2765 (2022).
[63] F. Wu, T. Lovorn, E. Tutuc, I. Martin, and A. H. MacDonald, Physical Review Letters **122**, 086402 (2019).
[64] N. Morales-Durán, N. Wei, and A. H. MacDonald, arXiv preprint arXiv:2308.03143 (2023).
[65] F. Xie, N. Regnault, D. Călugăru, B. A. Bernevig, and B. Lian, Physical Review B **104**, 115167 (2021).
[66] J. Wang, Y. Zheng, A. J. Millis, and J. Cano, Physical Review Research **3**, 023155 (2021).
[67] S. Becker, I. Oltman, and M. Vogel, arXiv preprint arXiv:2309.02701 (2023).
[68] M. Koshino, N. F. Yuan, T. Koretsune, M. Ochi, K. Kuroki, and L. Fu, Physical Review X **8**, 031087 (2018).
[69] J. Zang, J. Wang, A. Georges, J. Cano, and A. J. Millis, arXiv preprint arXiv:2210.11573 (2022).
[70] Z.-D. Song and B. A. Bernevig, Physical Review Letters **129**, 047601 (2022).
[71] Y.-H. Zhang, H. C. Po, and T. Senthil, Physical Review B **100**, 125104 (2019).
[72] Y. H. Kwan, G. Wagner, T. Soejima, M. P. Zaletel, S. H. Simon, S. A. Parameswaran, and N. Bultinck, Physical Review X **11**, 041063 (2021).
[73] D. E. Parker, T. Soejima, J. Hauschild, M. P. Zaletel, N. Bultinck, *et al.*, Physical Review Letters **127**, 027601 (2021).
[74] G. Wagner, Y. H. Kwan, N. Bultinck, S. H. Simon, and S. Parameswaran, Physical Review Letters **128**, 156401 (2022).
[75] X. Liu, G. Farahi, C.-L. Chiu, Z. Papic, K. Watanabe, T. Taniguchi, M. P. Zaletel, and A. Yazdani, Science **375**, 321 (2022).
[76] Y. Sheffer, R. Queiroz, and A. Stern, Physical Review X **13**, 021012 (2023).
[77] V. Crépel and A. Millis, arXiv preprint arXiv:2403.15546 (2024).
[78] H. Li, Y. Su, Y. B. Kim, H.-Y. Kee, K. Sun, and S.-Z. Lin, arXiv preprint arXiv:2402.02251 (2024).
[79] J. Kang and O. Vafek, Physical Review B **107**, 075408 (2023).
[80] O. Vafek and J. Kang, Physical Review B **107**, 075123 (2023).
[81] Z. Song, Z. Wang, W. Shi, G. Li, C. Fang, and B. A. Bernevig, Physical Review Letters **123**, 036401 (2019).

Appendix A: Invertible transformation

In this appendix, we assume that a constant of motion $\vec{X}\cdot\vec{\mu} = X_1\mu_1 + X_2\mu_2 + X_3\mu_3$ solution of

$$\left[\vec{X}\cdot\vec{\mu}, \mathcal{D}\right] = 0 \quad \Longleftrightarrow \quad \partial_{\bar{z}}\vec{X} + \alpha\vec{X}\times\vec{\mathcal{A}} = 0, \tag{A1}$$

exist in order to

- show that $\vec{X}\cdot\vec{X}$ is uniform in space and real.
- derive the form of the effective gauge potential A'_z appearing in Eq. 6.
- prove that $\vec{X}$ cannot be carried by μ_3 only away from high-symmetry points of the moiré unit cell.

1. Uniform and real x^2

We first demonstrate that $x^2 = \vec{X}\cdot\vec{X}$ is uniform and real. We can first easily show that it is holomorphic

$$\partial_{\bar{z}}(\vec{X}\cdot\vec{X}) = 2\vec{X}\cdot\partial_{\bar{z}}\vec{X} = -2\alpha\vec{X}\cdot(\vec{X}\times\mathcal{A}) = 0. \tag{A2}$$

Because x is also additionally periodic (due to the periodicity of $\mathcal{A}$), it must be constant (uniform in space). Then, we use the C_{2y} symmetry of the chiral Hamiltonian for TBG. This symmetry exchanges the layers and complex conjugates the gauge fields $A_z^{(j)} \to \left[A_z^{(j)}\right]^*$ for $j = 1, 2$, as can be derived from their explicit representation (Eq. 3). As a result, we find that $\vec{X}(-r_1, r_2) = \vec{X}^*(r_1, r_2)$, which ensures that all components of $\vec{X}$ are real on the y-axis where $r_1 = 0$ [we use (r_1, r_2) for the position instead of (x, y) to avoid confusion of the horizontal position with the $x^2 = \vec{X}\cdot\vec{X}$], which results in a real x^2.

2. Abelianization

We then perform the calculation of the transformed Dirac operators $\mathcal{D}' = U^{-1}\mathcal{D}U$ with

$$U = U^{-1} = \frac{1}{\sqrt{N}}(\vec{X}\cdot\vec{\mu} + x\mu_3), \quad N = 2x(x + X_3). \tag{A3}$$

A direct calculation gives

$$\begin{aligned}
\mathcal{D}' &= U^{-1}\mathcal{D}U, \\
&= \frac{1}{N}[(\vec{X}\cdot\vec{\mu})\mathcal{D}(\vec{X}\cdot\vec{\mu}) + x^2\mu_3\mathcal{D}\mu_3] + \frac{x}{N}[\mu_3\mathcal{D}(\vec{X}\cdot\vec{\mu}) + (\vec{X}\cdot\vec{\mu})\mathcal{D}\mu_3] + \sqrt{N}(-2i\partial_{\bar{z}}N^{-1/2})\mu_0 \\
&= \frac{1}{N}[\underbrace{(\vec{X}\cdot\vec{\mu})^2}_{x^2\mu_0}\mathcal{D} + x^2\mu_3\mathcal{D}\mu_3] + \frac{x}{N}[\mu_3(\vec{X}\cdot\vec{\mu})\mathcal{D} + (\vec{X}\cdot\vec{\mu})\mathcal{D}\mu_3] + \frac{i}{N}(\partial_{\bar{z}}N)\mu_0 \\
&= \frac{x^2}{N}[2\cdot(-2i\partial_{\bar{z}})\mu_0] + \frac{x}{N}[\underbrace{\{\mu_3, \vec{X}\cdot\vec{\mu}\}}_{2X_3}(-2i\partial_{\bar{z}}) + \underbrace{[\mu_3, \vec{X}\cdot\vec{\mu}]}_{2i(\hat{u}_3\times\vec{X})\cdot\vec{\mu}}(\alpha\vec{\mathcal{A}}\cdot\vec{\mu})] + \frac{2ix}{N}(\partial_{\bar{z}}X_3)\mu_0 \\
&= \frac{2x(x + X_3)}{N}(-2i\partial_{\bar{z}})\mu_0 - \frac{2ix}{N}[(\partial_{\bar{z}}X_3)\mu_0 + i\alpha(\vec{X}\cdot\vec{\mathcal{A}})\mu_3] + \frac{2ix}{N}(\partial_{\bar{z}}X_3)\mu_0 \\
&= (-2i\partial_{\bar{z}})\mu_0 + \frac{\alpha(\vec{X}\cdot\vec{\mathcal{A}})}{x + X_3}\mu_3,
\end{aligned} \tag{A4}$$

where the first line is a simple re-ordering, the second line uses the fact that $(\vec{X}\cdot\mu)$ commutes with $\mathcal{D}$, the third uses that $\vec{\mathcal{A}}$ has no μ_3 component such that $\mu_3(\vec{\mathcal{A}}\cdot\vec{\mu})\mu_3 = -(\vec{\mathcal{A}}\cdot\vec{\mu})$, the fourth and fifth simplify the products of Pauli matrices. This represents two decoupled copies subject, each subject to an abelian $U(1)$ gauge field

$$\pm A'_z = \pm\frac{\alpha(\vec{X}\cdot\vec{\mathcal{A}})}{x + X_3}, \tag{A5}$$

that is opposite for the two copies.

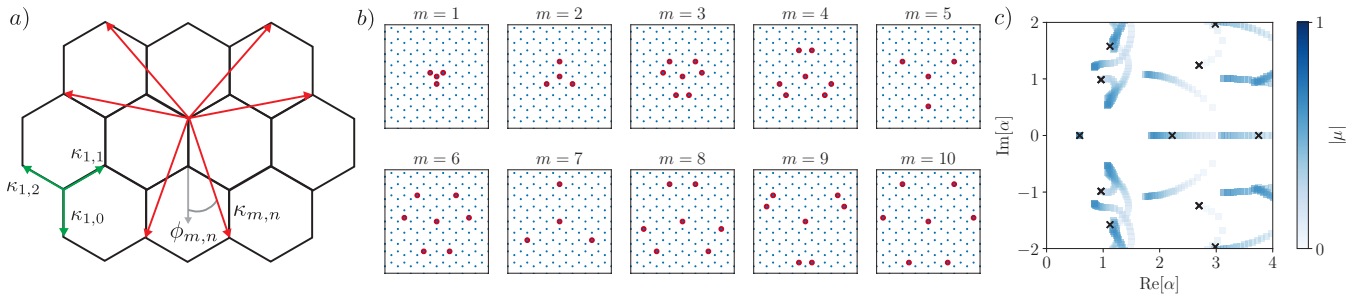

FIG. 8. a) Definition of the angle $\phi_{m,n}$ as the polar angle of $\kappa_{m,n}$, measured from the negative y-axis, represented for the the $m = 3$ harmonics (red arrows). We also show the lowest harmonics corresponding to the tunneling in the Bistritzer-MacDonald model in green. b) Definition of the $\kappa_{m,n}$ vectors, which start from the origin and point to the red dots. c) The flow of magic angles on the complex plane as a function of increasing disorder strength $|\mu|$ (color bar) while $\hat{\mu}$ is fixed. We put disorder in the first 6 channels and use a truncation $R_k = 20\sqrt{3}\kappa$.

3. Out-of-plane constant of motion

We finally prove by contradiction that $\vec{X} \cdot \vec{\mu}$ cannot be purely carried by μ_3 at a point r_0 away from the origin and corners of the Wigner-Seitz moiré unit cell. We will rely on the fact that x is constant and reason by contradiction. Assume that we can write $\vec{X}(r_0) \cdot \vec{\mu} = x\mu_3$. Then, consider a small displacement $\eta = (\eta_x, \eta_y)$ away from this point. The equation defining the constant of motion Eq. A1 gives $X_1(r_0 + \eta) = -x\alpha A_z^{(1)}(r_0)\bar{\eta}$, $X_2(r_0 + \eta) = x\alpha A_z^{(2)}(r_0)\bar{\eta}$, and $X_3(r_0 + \eta) = x$ with $\bar{\eta} = \eta_x - i\eta_y$. For the norm x^2 to be constant, we therefore need that $x^2 = x^2[1 + \alpha^2\bar{\eta}^2[(A_z^{(1)})^2(r_0) + (A_z^{(2)})^2(r_0))]$, which requires $(A_z^{(1)})^2(r_0) + (A_z^{(2)})^2(r_0) = 0$. This is only true for the field in Eq. 3 at the origin and corners of the Wigner-Seitz moiré unit cell, providing the desired contradiction.

Appendix B: Numerical determination of magic angles

In this Appendix, we provide details on our numerical simulation of disorder in the chiral TBG Hamiltonian. We use the method introduced in Ref. [56], which we briefly summarize here for completeness.

We begin by describing the chiral model without disorder. The Hamiltonian can be written as

$$\mathcal{H}_{\mathrm{D}} = \begin{pmatrix} 0 & \mathcal{D} \\ \mathcal{D}^\dagger & 0 \end{pmatrix}, \quad \text{where} \quad \mathcal{D} = \begin{pmatrix} \hat{D} & \alpha\hat{T}_- \\ \alpha\hat{T}_+ & \hat{D} \end{pmatrix} \tag{B1}$$

and $\hat{T}_\pm = \hat{T}(\pm z)$ is the inter-layer hopping written in terms of the complex variable $z = x + iy$. The tunneling potential $\hat{T}$ is related to the gauge field $\mathcal{A}_z$ defined in Eq. 3 of the main text by

$$\hat{T}(z) = A_z^{(1)} + iA_z^{(2)} = \sum_{n=0,1,2} \omega^n \exp(i\kappa_n \cdot r) \tag{B2}$$

with $\omega = e^{i2\pi/3}$, and where $\kappa_n \equiv \kappa_{1,n}$ are the three smallest vectors connecting the two corners of the moiré Brillouin zone, represented with green arrows in Fig. 8a. We consider the effects of disorder in the inter-layer tunneling potential $\hat{T}_\pm$ through the addition of a perturbation that we decompose in harmonics labeled by m

$$\hat{T} \to \hat{T} + \sum_m \mu_m \hat{T}_m \tag{B3}$$

where $\{\mu_m\}$ is a random vector of small norm $|\mu| = [\sum_m \mu_m^2]^{1/2} \ll 1$. The wave-vectors corresponding to the smallest ten harmonics ($m \leq 10$) are depicted in Fig. 8b. These channels were used in Fig. 6 of the main text as well. Notice that, for each m, there are several wave-vectors of equal norm related by C_3 and/or C_{2y} symmetry that contribute to $\hat{T}_m$. We denote them as $\kappa_{m,n}$, with n an auxiliary index taking either three or more distinct values depending on the number of nonequivalent wave-vectors in the m-th harmonic (compare for instance $m = 2$ and $m = 3$ in Fig. 8b). In

the main text, we considered perturbations $\hat{T}_m$ that preserve the C_3 and C_{2y} symmetry of the chiral Hamiltonian for TBG (Eq. 3), which constrains the functional form of these inter-layer tunneling terms to

$$\hat{T}_m = a^{(1)}_{m,z} + i a^{(2)}_{m,z} = \sum_n e^{i(\kappa_{m,n}\cdot r + \phi_{m,n})}. \tag{B4}$$

As illustrated in Fig. 8a and b, these terms can be interpreted as long-range tunnelings in momentum space, with an amplitude equal to μ_m, a direction given by $\kappa_{m,n}$, and a phase $\phi_{m,n}$. Amongst all gauge equivalent choices for the $\phi_{m,n}$ phases leading to C_3 and C_{2y} symmetric $\hat{T}_m$, we choose the one where $\phi_{m,n}$ is the polar angle of $\kappa_{m,n}$ measured from the negative y-axis, as illustrated in Fig. 8a. The main advantage of this prescription is that it equally applies to harmonics containing three and six wave-vectors (Fig. 8b).

The problem of finding the magic angle corresponds to finding vectors $|\psi\rangle$ and $|\chi\rangle$ such that

$$\begin{pmatrix} \hat{D} & \alpha\hat{T}_- \\ \alpha\hat{T}_+ & \hat{D} \end{pmatrix} \begin{pmatrix} |\psi\rangle \\ |\chi\rangle \end{pmatrix} = 0 \quad \Rightarrow \quad \Lambda|\psi\rangle = \frac{1}{\alpha^2}|\psi\rangle, \quad \Lambda = \hat{D}^{-1}\hat{T}_+\hat{D}^{-1}\hat{T}_-, \tag{B5}$$

which itself reduces to finding the eigenvalues $\{\lambda_i\}$ of the (non-Hermitian) operator Λ. The magic angles $\{\alpha_i\}$ are then calculated as $\alpha_i = 1/\sqrt{\lambda_i}$. The operators $\hat{D}$ and $\hat{T}_\pm$ can be represented as sparse matrices on a momentum space grid and are, in practice, truncated by removing all momenta with norm higher than a certain cutoff R_k.

As an illustration of the method, we introduce disorder in the first $m_c = 6$ channels using $\vec{\mu} = |\mu|\hat{\mu}$, varying the overall strength of the disorder $|\mu|$ for a fixed random vector normalized to unity $\hat{\mu}$. In Fig. 8c, we show the evolution of the magic angles$\{\alpha_i\}$ on the complex plane as a function of increasing disorder strength $|\mu|$. We see that only the first magic angle is robust against the perturbation, while all the other magic angles are dramatically changed as disorder strength increases.

Appendix C: Small Momentum Perturbation

The inter-layer tunneling decomposed into higher harmonic $m \geq 1$ of Eq. B3 can only describe disorder with a correlation length smaller than moiré unit cell. In this Appendix, we explore the opposite regime where the disorder correlation length is larger than the moiré unit cell. Physically, twist angle variations across the sample belong to this class of perturbations.

Introducing harmonics that are periodic on an enlarged moiré unit cell in real space requires access to wave-vectors that are fractions of the original $\kappa_{1,n}$ appearing in the Bistritzer-MacDonald model (Eq. 3). To achieve this numerically, we rescale the momentum-space lattice of Fig. 8b by a factor $r = 1/M$, with $M = 3p + 1$ and $p \in \mathbb{Z}$. This choice ensures that the reduced lattice still contains the $\kappa_{1,n}$. By convention, rescaling by a negative value r corresponds to a rescaling by $|r| > 0$ followed by a 180° degree rotation, as illustrated in Fig. 9a for the case $r = -1/2$ (corresponding to $M = -2$, $p = -1$). The inter-layer harmonics $\hat{T}'_m$ on the rescaled lattice with wave-vectors $\kappa'_{m,n}$ can now be used to introduce disorder with correlation length larger than the moiré lattice constant. The definitions of $\hat{T}'_m$ and $\kappa'_{m,n}$ are the same as $\hat{T}_m$ and $\kappa_{m,n}$ (see App. B), albeit on the rescaled honeycomb lattice. We also highlight that $\kappa_{1,n} = \kappa'_{|M|,n}$, which is also illustrated in Fig. 9a.

We reproduce the calculation of Fig. 6a for the fractional wave-vectors $\kappa'_{m,n}$ and consider an inter-layer tunneling of the form

$$\hat{T}' = \hat{T}'_{|M|} + \delta\mu\hat{T}'_1, \tag{C1}$$

where $\hat{T}'_{|M|}$ is nothing but the terms appearing in the un-perturbed chiral Hamiltonian for TBG (Eq. 3), while $\hat{T}'_1$ is the lowest accessible fractional harmonic on the rescaled lattice. The latter realizes a perturbation of momentum $q_{\text{pert}} = |\kappa/M|$. In Fig. 9b, we show the derivative of the magic angles $|\partial\alpha/\partial\mu|$, numerically computed using a small disorder strength $\delta\mu = 0.02$ (see Sec. IV B), for the first three magic angles as a function of $M = \left|\frac{\kappa}{q_{\text{pert}}}\right| = \left|\frac{\kappa}{\kappa'_{1,0}}\right|$. We observe that, unlike the perturbation of larger momentum where only the first magic angle enjoyed protection, all magic angles respond similarly to disorder. Thus, there is no special protection of the first magic angle against perturbations of correlation length longer than the moiré lattice vector.

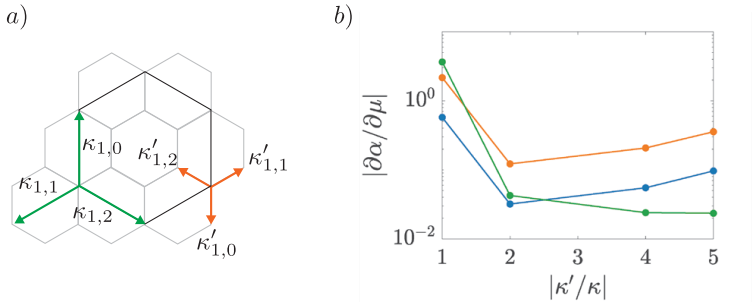

FIG. 9. a) Illustration of the rescaled honeycomb lattice for $M = -2$ (grey) lines. The rescaled lattice is generated by the basis vectors $\kappa'_{1,n}$ with $|\kappa'_{1,n}| = |\kappa|/2$, and contains the wave-vectors $|\kappa_{1,n}|$ appearing in the Bistritzer-Macdonald model. The original moiré Brillouin zone is drawn in black. b) Variation $|\partial\alpha/\partial\mu|$ of the first (blue), second (orange), and third (green) magic angle, numerically evaluated using $\delta\mu = 0.02$, as a function of $M = \left|\frac{\kappa}{q_{\rm pert}}\right| = \left|\frac{\kappa}{\kappa'_{1,0}}\right|$. To obtain converged results for large m, we used a large truncation radius $R_k = 35\sqrt{3}|\kappa|$.